Thin-film flow in helically-wound rectangular channels with small torsion

Y. M. Stokes*

School of Mathematical Sciences, The University of Adelaide, SA 5005, AUSTRALIA

B. R. Duffy† and S. K. Wilson‡

Department of Mathematics and Statistics,

University of Strathclyde, Livingstone Tower,

26 Richmond Street, Glasgow G1 1XH, UNITED KINGDOM

H. Tronnolone§

School of Mathematical Sciences, The University of Adelaide, SA 5005, AUSTRALIA

(Dated: June 25, 2013)

Abstract

Laminar gravity-driven thin-film flow down a helically-wound channel of rectangular cross-section with small torsion in which the fluid depth is small is considered. Neglecting the entrance and exit regions we obtain the steady-state solution that is independent of position along the axis of the channel, so that the flow, which comprises a primary flow in the direction of the axis of the channel and a secondary flow in the cross-sectional plane, depends only on position in the two-dimensional cross-section of the channel. A thin-film approximation yields explicit expressions for the fluid velocity and pressure in terms of the free-surface shape, the latter satisfying a non-linear ordinary differential equation that has a simple exact solution in the special case of a channel of rectangular cross-section. The predictions of the thin-film model are shown to be in good agreement with much more computationally intensive solutions of the small-helix-torsion Navier–Stokes equations. The present work has particular relevance to spiral particle separators used in the mineral-processing industry. The validity of an assumption commonly used in modelling flow in spiral separators, namely that the flow in the outer region of the separator cross-section is described by a free vortex, is shown to depend on the problem parameters.

* Corresponding author: yvonne.stokes@adelaide.edu.au

† b.r.duffy@strath.ac.uk

‡ s.k.wilson@strath.ac.uk

§ hayden.tronnolone@adelaide.edu.au

I. INTRODUCTION

Flows in curved geometries, such as those that arise in many piping systems, and, in particular, in the human blood-circulation system, have motivated study of fully-developed flow in completely filled helically-wound pipes. A common assumption is that the flow is helically symmetric, which here means that there is a steady-state solution that is independent of position along the axis of the pipe. Thus the flow, which comprises a primary flow along the axis and a secondary flow in the cross-sectional plane normal to the axis, depends only on position in the two-dimensional cross-section of the pipe [1–5]. In the present work we consider flows in helically-wound channels (see Figure 1) which differ from their filled-pipe counterparts in having a free surface. They have been studied in the contexts of river flow and sediment transport [6–8], distillation of petroleum products [9, 10] and, of particular interest here, spiral particle separation [11–18, 22–25].

Spiral particle separators are helically-wound channels along which particle-laden slurries flow under gravity. They are used in the coal and mineral-processing industries to segregate and concentrate particles of different sizes and densities [12, 26]. Theoretical understanding of these devices has lagged practical development and, although considerable progress towards filling this gap has been made over the past four decades, the lack of a good "quantitative basis for the design and evaluation of spiral separators" [12] largely remains to this day. A steady-state empirical mathematical model was developed by Holland-Batt [11, 25], in which the primary flow down the channel is described by a Manning law in an inner region near the central column around which the channel is wound, and a free vortex in the outer region. The transition point between the two regions is specified empirically, with a smoothing function used to avoid discontinuities; for details see Holland-Batt [11]. Flow-visualisation experiments performed by Hotham [12, 14] and Holland-Batt and Holtham [13] to validate this model proved to be difficult, but did confirm the existence of the predicted secondary flow, in addition to showing that the fluid depth is small, that some flow regions are turbulent, and that the flow reaches a fully-developed profile within two spiral turns, as well as giving rough estimates of flow velocities.

Computational Fluid Dynamics (CFD) simulations of steady laminar flow in a spiral separator seem to have been performed first by Wang and Andrews [15]; helical symmetry was assumed, and the flow in a planar cross-section of the channel was determined via a finite

difference method. Three-dimensional CFD simulations of laminar flow were performed by Jancar et al. [16] using the finite-volume method, and turbulence models were included by Matthews et al. [17, 18], who used the volume-of-fluid method.

All the above studies are in agreement that in order to improve the operation of spiral separators it is necessary to have a better understanding of the flow in them, and, in particular, to obtain a quantitative understanding of the influences of fluid properties and of geometrical parameters (such as the curvature and torsion of the helical channel axis, and the channel cross-sectional geometry) on the flow; the purpose of the present paper is to develop an alternative model for this flow (and for other helical flows of similar types), based on the observation that the fluid depth is small but centrifugal effects are significant, in general. We then verify this approach via comparison with numerical solutions of the full problem, and investigate the predictions of the thin-film theory in detail.

The work of Holland-Batt and Holtham [12–14] shows that over most of the channel the flow is laminar; this motivates the use of a laminar model, as considered herein. (Indeed, the laminar and turbulence models of Holland-Batt and Holtham are not too dissimilar from each other.) However, Holland-Batt's suggestion of a free-vortex primary flow (either in the outer region [11, 13] or across the entire channel [25]) is inconsistent with some of the experimental observations of Holland-Batt and Holtham [13], because the predicted free-surface shape has the wrong curvature in the outer region; the present model seems to capture the observed curvature correctly, although quantitative comparison with the experiments is difficult because, as Holtham [14] acknowledges, the experimental measurements that he reports are prone to significant errors. Holland-Batt [25] adopts the free-vortex model even for spiral separators of large diameter, a case in which, according to the present model, it is unlikely to be valid.

In the present work we consider laminar gravity-driven thin-film flow in a helically-wound channel. We assume that the helical channel axis has small torsion, an assumption that is appropriate for spiral particle separators, and seek a helically-symmetric steady-state solution for the flow. As part of the solution process, the free-surface shape of the fluid in the channel must be determined, making this analysis significantly different from and more complicated than that for fully-developed flows in filled pipes. Since the channels of spiral particle separators typically have widths of the order of half a metre, two orders of magnitude larger than the capillary length scale at which surface tension is important (of

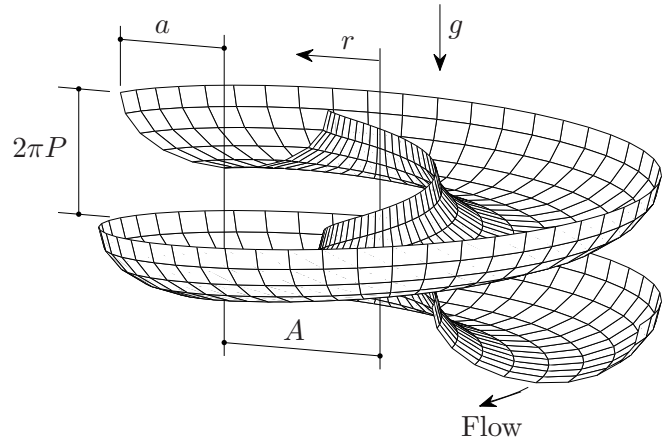

FIG. 1. A right-handed helically-wound channel. The central axis of the channel is a helix of radius A and pitch $2\pi P$. The fluid-filled portion of the channel has width $2a$.

the order of a few millimetres for water), we are justified in neglecting the effect of surface tension. In Section II we describe the helically-symmetric small-torsion model for flows of arbitrary depth and discuss the numerical solution of this model. Then, since flows in spiral separators are typically shallow, in Section III we derive a thin-film model, which we verify using the more general model described in Section II. Related work on the flow of a thin rivulet down a locally non-planar substrate (but in which surface-tension effects are significant) has been performed by Wilson and Duffy [20, 21]. In Section IV we use the thin-film model to examine thin-film flow in helically-wound channels of rectangular cross-section. Some preliminary work on deeper flows has been performed by Stokes [22, 23]. Finally, in Section V we summarise our results and draw some conclusions (which we anticipate are also relevant to helical flows with a free surface other than those occurring in particle separators).

II. HELICALLY-SYMMETRIC SMALL-HELIX-TORSION MODEL

A. Governing equations

Consider steady gravity-driven flow of a prescribed volume flux Q of fluid of constant density ρ and viscosity μ down a helically-wound channel whose central axis is a vertical right-handed helix with radius A and pitch $2\pi P$ (see Figure 1). The fluid-filled portion of the channel is taken to be $A + y_\ell \leq r \leq A + y_r$, where r denotes the radial coordinate indicated in Fig. 1, and y_ℓ and y_r correspond to the positions of the left-hand and right-hand ends of

the free surface, respectively, so that the fluid occupies a width $2a = y_r - y_\ell$ of the channel. (In particular, later in the present study we consider a channel of rectangular cross-section of width $2a$, for which we take $-y_\ell = y_r = a$.)

Let α be the angle of inclination of the helix to the horizontal, given by $\tan\alpha = P/A$. We define the dimensionless curvature and torsion of the helix, ϵ and τ, and the dimensionless Reynolds and Froude numbers of the flow, R and F, by

$$\epsilon = \frac{aA}{A^2 + P^2}, \quad \tau = \frac{aP}{A^2 + P^2}, \quad R = \frac{\rho U a}{\mu}, \quad F = \frac{U}{\sqrt{ga}}, \tag{1}$$

where U is a characteristic axial velocity (specified in Section III, after the thin-film model has been introduced) and g is the magnitude of gravitational acceleration, and we note that $\tan\alpha = P/A = \tau/\epsilon$. Physically we require $A \geq a$, to avoid self-intersection of the channel. This immediately implies from (1) that $\epsilon < 1$ for any $\tau > 0$. Spiral particle separators used in the mineral-processing industry typically have $\epsilon \simeq 0.2 - 0.5$ and $\tau \simeq 0.03 - 0.11$, and so in the present work we will consider spiral channels with $0 < \epsilon < 1$ in the small-torsion limit ($\tau \to 0$). Note that torsion was also assumed to be small in the early work by Dean [27] on flow in curved pipes. For flow in a channel the assumption of small torsion implies that the pitch of the helix is much larger than the fluid depth, and so the free surface will not intersect the portion of the channel directly above. This is consistent with the fact that fluid depths in spiral separators are small [12].

In studies of flow in helically-wound filled pipes with non-zero torsion [1, 3–5] considerable attention has been given to the selection of an appropriate orthogonal helical coordinate system. The essentially identical coordinate systems of Germano [1, 4] and Kao [3] identify a point in the flow domain by its local position in the cross-sectional plane normal to the vector tangent to the central helical pipe axis and the arc-length distance of the cross-section along this axis, which is valid for $\epsilon < 1$. In general, for such coordinate systems the assumption of helical symmetry means, in fact, that the flow is independent of the arc-length coordinate, which, as discussed by Zabielski and Mestel [5], is not true helical symmetry. They therefore propose a different coordinate system, formally equivalent to that of Germano and Kao, but which permits true helical symmetry. However, in the small torsion limit $\tau \to 0$, as considered in the present study, these coordinate systems are equivalent, and a flow that is independent of arc length along the central axis is truly helically symmetric. Thus, for simplicity, we adopt a coordinate system (x, y, z) similar to that used by Germano [1, 4]

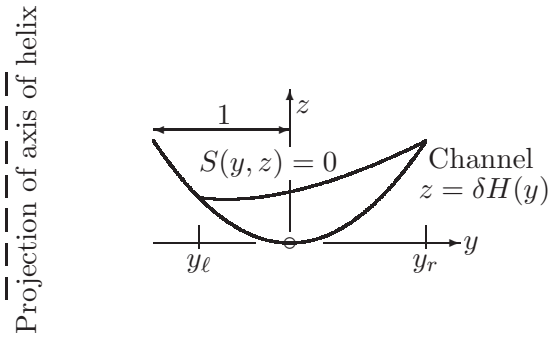

FIG. 2. Cross-section of a channel showing the locally Cartesian (x, y, z) coordinate system. The x-axis is directed out of the figure in the direction of the primary axial flow.

and Kao [3], in which x is arc length measured along the central axis of the helically-wound channel in the direction of the primary flow, and y and z are local Cartesian coordinates in the cross-sectional plane, as shown in Figure 2.

The steady helically-symmetric Navier–Stokes equations in the small-torsion limit ($\tau \to 0$) may be derived directly in terms of the present helical coordinates (x, y, z) using the vector differential quantities given by Batchelor [19, Appendix 2] in general curvilinear coordinates, in the same manner as Germano [1]; the scale factors corresponding to the x, y and z coordinates are $h_x = 1 + \epsilon y$, $h_y = 1$ and $h_z = 1$, respectively. Alternatively, we may start with the small-torsion limit of the fluid-flow equations given by Germano [1, 4], to which we add the gravitational force terms, and convert from the spatial (s, r, θ) coordinates used by Germano to the (x, y, z) coordinates used herein, using the transformation $(x, y, z) = (-s, r\sin\theta, r\cos\theta)$. For helically symmetric flow in a channel the velocity and pressure are independent of arc length ($x = -s$), with the flow being driven by gravity; this differs from a filled pipe, in which the flow may instead be driven by a prescribed pressure gradient along the axis of the pipe.

Let $\mathbf{u}(y, z) = (u(y, z), v(y, z), w(y, z))$ and $p = p(y, z)$ be the velocity vector and pressure, respectively, in the (x, y, z) coordinate system, with u corresponding to the primary (axial) flow, and v and w corresponding to the secondary (transverse) flow. In terms of the dimensionless variables

$$(\tilde{x}, \tilde{y}, \tilde{z}) = \left(\frac{x}{a}, \frac{y}{a}, \frac{z}{a}\right), \quad (\tilde{u}, \tilde{v}, \tilde{w}) = \left(\frac{u}{U}, \frac{Rv}{U}, \frac{Rw}{U}\right), \quad \tilde{p} = \frac{R^2(p - p_a)}{\rho U^2}, \tag{2}$$

where p_a is the constant atmospheric pressure, and with the tildes on dimensionless variables omitted for clarity, the continuity equation is

$$\frac{\partial}{\partial y}[(1 + \epsilon y)v] + \frac{\partial}{\partial z}[(1 + \epsilon y)w] = 0, \tag{3}$$

and the Navier–Stokes equations are

$$v\frac{\partial u}{\partial y}+w\frac{\partial u}{\partial z}=\frac{\partial^2 u}{\partial y^2}+\frac{\partial^2 u}{\partial z^2}-\frac{\epsilon}{1+\epsilon y}\left(uv-\frac{\partial u}{\partial y}+\frac{\epsilon u}{1+\epsilon y}\right)+\frac{R\sin\alpha}{F^2}, \tag{4a}$$

$$v\frac{\partial v}{\partial y}+w\frac{\partial v}{\partial z}-\frac{Ku^2}{2(1+\epsilon y)}=-\frac{\partial p}{\partial y}+\frac{\partial^2 v}{\partial y^2}+\frac{\partial^2 v}{\partial z^2}+\frac{\epsilon}{1+\epsilon y}\left(\frac{\partial v}{\partial y}-\frac{\epsilon v}{1+\epsilon y}\right), \tag{4b}$$

$$v\frac{\partial w}{\partial y}+w\frac{\partial w}{\partial z}=-\frac{\partial p}{\partial z}+\frac{\partial^2 w}{\partial y^2}+\frac{\partial^2 w}{\partial z^2}+\frac{\epsilon}{1+\epsilon y}\frac{\partial w}{\partial y}-\frac{R^2\cos\alpha}{F^2}, \tag{4c}$$

where $K=2\epsilon R^2$ is the dimensionless Dean number.

Equations (3) and (4) are to be integrated subject to no-slip and no-penetration boundary conditions on the channel walls, and continuity-of-stress and kinematic conditions on the free surface. Thus on the channel walls we have simply

$$u=v=w=0. \tag{5}$$

On the free surface the stress condition takes the form $-p\,\mathbf{n}+2\mathbf{e}\cdot\mathbf{n}=\mathbf{0}$, where $\mathbf{n}$ denotes the unit normal vector to the free surface, and $\mathbf{e}$ denotes the rate-of-strain tensor, whose components in helical coordinates may be obtained from the expressions given by, for example, Batchelor [19] or Yuan [29]. For a free surface $S(y,z)=0$ a normal vector is given by

$$\mathbf{n}=(n_x,n_y,n_z)=\nabla S=\left(0,\frac{\partial S}{\partial y},\frac{\partial S}{\partial z}\right), \tag{6}$$

and the continuity-of-stress boundary conditions at the free surface are

$$\left(\frac{\partial u}{\partial y}-\frac{\epsilon}{1+\epsilon y}u\right)n_y+\frac{\partial u}{\partial z}n_z=0, \tag{7a}$$

$$\left(-p+2\frac{\partial v}{\partial y}\right)n_y+\left(\frac{\partial w}{\partial y}+\frac{\partial v}{\partial z}\right)n_z=0, \tag{7b}$$

$$\left(\frac{\partial w}{\partial y}+\frac{\partial v}{\partial z}\right)n_y+\left(-p+2\frac{\partial w}{\partial z}\right)n_z=0. \tag{7c}$$

In addition to the above, the kinematic condition at the free surface, $\mathbf{u}\cdot\nabla S=0$, gives

$$v\frac{\partial S}{\partial y}+w\frac{\partial S}{\partial z}=0. \tag{8}$$

The governing equations and boundary conditions (3)–(8) are to be solved for some prescribed value of the volume flux Q down the channel to give the velocity and pressure distributions in the flow domain and the free-surface shape $S(y,z)=0$. We denote the cross-sectional area of the flow domain by Ω.

From (3) we see that the secondary flow may be represented in terms of a stream function $\psi = \psi(y, z)$ defined by

$$\frac{\partial \psi}{\partial z} = (1 + \epsilon y)v, \quad \frac{\partial \psi}{\partial y} = -(1 + \epsilon y)w, \tag{9}$$

together with the condition that $\psi = 0$ on the boundary of the flow domain.

B. Numerical solutions

In general, the model described above must be solved numerically, and for this we may use a general-purpose CFD package. Previously, a method employing the finite-element package Fastflo (developed by the CSIRO, Australia) was discussed and demonstrated by Stokes [22, 23]. In the present work we instead make use of the commercial finite-element package COMSOL Multiphysics.

Starting with an initial estimate of the free-surface shape, the problem is solved iteratively, with the free-surface shape adjusted at each iteration, until a steady state solution is obtained. In the present work we are considering flows of small depth, and an excellent estimate of the free-surface shape is given by the thin-film model described subsequently in Section III. In particular, the points of contact of the free surface with the channel walls are taken to be as given by the thin-film model, so that the difficulty of determining these, discussed by Stokes [22, 23], is resolved. As will be shown, with the thin-film model providing the initial flow domain for the numerical solution process, a numerical solution of very good accuracy can be obtained. A detailed description of the setup and solution process is given in Appendix A.

III. THIN-FILM MODEL

A. Derivation

As mentioned earlier, flows in spiral particle separators are typically of small depth. We now exploit this to derive a thin-film model for a channel of general shape by a perturbation expansion in terms of a small parameter $\delta \ll 1$ representative of the cross-sectional aspect ratio of the flow.

We first define new variables (denoted by carets) by

$$z = \delta\hat{z}, \quad v = R\delta\hat{v}, \quad w = R\delta^2\hat{w} \quad \text{and} \quad p = \frac{R\hat{p}}{\delta}, \tag{10}$$

and choose $\delta^2 R/F^2 = 1$, i.e. $\delta = F/\sqrt{R} = \sqrt{\nu U/(ga^2)}$, where $\nu = \mu/\rho$, which explicitly defines the parameter δ in terms of the physical parameters. We return to this definition in a more detailed examination of the scaling of the model in the next Subsection. Substituting (10) into equations (3) and (4) gives, at leading order in δ,

$$\frac{\partial}{\partial y}[(1+\epsilon y)\hat{v})] + \frac{\partial}{\partial \hat{z}}[(1+\epsilon y)\hat{w}] = 0, \tag{11a}$$

$$\frac{\partial^2 u}{\partial \hat{z}^2} + \sin\alpha = 0, \tag{11b}$$

$$-\frac{\partial \hat{p}}{\partial y} + \frac{\partial^2 \hat{v}}{\partial \hat{z}^2} + \frac{\chi}{1+\epsilon y}u^2 = 0, \tag{11c}$$

$$-\frac{\partial \hat{p}}{\partial \hat{z}} - \cos\alpha = 0, \tag{11d}$$

where the parameter $\chi = \delta K/(2R)$ is taken to be $O(1)$. Equations (11b)–(11d) represent balances between viscosity and gravity in the x direction, pressure gradient, viscosity and centrifugal force in the y direction, and pressure gradient and gravity in the z direction, respectively. Under this thin-film scaling, the boundary conditions on the free surface $\hat{S}(y,\hat{z}) = 0$ become, at leading order in δ,

$$\frac{\partial u}{\partial \hat{z}} = 0, \quad \frac{\partial \hat{v}}{\partial \hat{z}} = 0, \quad \hat{p} = 0 \quad \text{and} \quad \hat{v}\frac{\partial \hat{S}}{\partial y} + \hat{w}\frac{\partial \hat{S}}{\partial \hat{z}} = 0. \tag{12}$$

Let the cross-section of the channel be of general shape $\hat{z} = H(y)$ and let the fluid depth be $h(y)$, so that the free surface is at $\hat{z} = H(y) + h(y)$. Integrating (11b) and (11d), substituting u and $\hat{p}$ into (11c) and integrating for $\hat{v}$ we obtain

$$u = \frac{\sin\alpha}{2}\,(\hat{z}-H)(H+2h-\hat{z}), \tag{13a}$$

$$\hat{v} = -\frac{\chi\sin^2\alpha}{120(1+\epsilon y)}\,(\hat{z}-H)\left[(\hat{z}-H)^5 - 6h(\hat{z}-H)^4 + 10h^2(\hat{z}-H)^3 - 16h^5\right] - \frac{\cos\alpha}{2}(\hat{z}-H)(H+2h-\hat{z})\frac{\mathrm{d}}{\mathrm{d}y}(H+h), \tag{13b}$$

$$\hat{p} = \cos\alpha\,(H+h-\hat{z}). \tag{13c}$$

Rewriting the continuity equation (11a) in the alternative form

$$\int_H^{H+h} \hat{v}\,\mathrm{d}\hat{z} = 0, \tag{14}$$

substituting for $\hat{v}$, and integrating yields a first-order ordinary differential equation (ODE) for h for a general prescribed channel shape $\hat{z} = H(y)$:

$$\frac{\mathrm{d}}{\mathrm{d}y}(H+h) = \frac{h^4}{1+\epsilon y}. \tag{15}$$

In writing (15) we have set $6\chi \sin^2\alpha/(35\cos\alpha) = 1$, which scales the problem as described in the next Subsection. Note that the ODE (15) explicitly involves the helix curvature ϵ, but is independent of other parameters.

Substituting (15) in (13b) yields

$$\hat{v} = \frac{\cos\alpha}{144(1+\epsilon y)}(\hat{z}-H)(H+2h-\hat{z})\left\{7\left[(H+h-\hat{z})^2-2h^2\right]^2-23h^4\right\} \tag{16}$$

from which it is straightforward to show that the flow is outward ($\hat{v} > 0$) on and near the free surface $\hat{z} = H + h$, but is inward ($\hat{v} < 0$) near the channel wall $\hat{z} = H$. Thus, in general, the secondary flow comprises one or more eddies in each of which the flow is always clockwise, regardless of the channel shape $\hat{z} = H(y)$.

From (9) the stream function for the secondary flow $\hat{\psi}$ is defined by $\partial\hat{\psi}/\partial\hat{z} = (1+\epsilon y)\hat{v}$ and $-\partial\hat{\psi}/\partial y = (1+\epsilon y)\hat{w}$. Substituting for $\hat{v}$ and integrating subject to $\hat{\psi} = 0$ on $\hat{z} = H(y)$ we obtain

$$\hat{\psi} = \frac{\cos\alpha}{144}(\hat{z}-H)^2(H+2h-\hat{z})^2(H+h-\hat{z})\left[(H+h-\hat{z})^2-5h^2\right]. \tag{17}$$

The scaled cross-sectional area of the flow domain, $\hat{\Omega} = \Omega/\delta = \Omega\, R^{1/2}/F$, is given by

$$\hat{\Omega} = \int_{y_\ell}^{y_r} h\,\mathrm{d}y, \tag{18}$$

and the scaled volume flux down the channel, $\hat{Q} = Q/(\delta\sin\alpha) = Q\,R^{1/2}/(F\sin\alpha)$, is given by

$$\hat{Q} = \frac{1}{\sin\alpha}\int_{y_\ell}^{y_r}\int_{H}^{H+h} u\,\mathrm{d}\hat{z}\,\mathrm{d}y = \frac{1}{3}\int_{y_\ell}^{y_r} h^3\,\mathrm{d}y, \tag{19}$$

where again $y = y_\ell$ and $y = y_r$ are the positions of the left-hand and right-hand ends of the free surface, respectively. To obtain a thin-film solution for a given channel shape $\hat{z} = H(y)$ we must solve (15) subject to a prescribed flux $\hat{Q} = \mathcal{Q}$, with $\hat{Q}$ given by (19).

We let $h(y_\ell) = h_\ell$ and $h(y_r) = h_r$ denote the fluid depth at the left-hand and right-hand end of the free surface, respectively, so that (y_ℓ, h_ℓ) and (y_r, h_r) are the points of contact of the free surface with the channel wall. For any channel geometry, two of the four values y_ℓ, y_r, h_ℓ, h_r will be known and two must be determined as part of the solution of the problem.

Once the fluid depth h has been determined it is straightforward to obtain $\hat{\psi}$, u, $\hat{v}$, $\hat{w}$ and $\hat{p}$ by substituting for H and h in the formulae given above.

B. Scaling of the model

In deriving the thin-film model in the previous Subsection we set

$$\frac{\delta^2 R}{F^2} = 1 \quad \text{and} \quad \frac{6\chi \sin^2\alpha}{35\cos\alpha} = 1, \tag{20}$$

and claimed that this corresponds to a particular scaling of the model. In this Subsection we describe this scaling in more detail.

Since $\chi = \delta K/(2R) = \delta\epsilon R = 35\cos\alpha/(6\sin^2\alpha)$ and $\delta = FR^{-1/2}$ we find that

$$\frac{35\cos\alpha}{6\epsilon\sin^2\alpha} = FR^{1/2}. \tag{21}$$

Then, substituting $FR^{-1/2} = \sqrt{\nu U/(ga^2)}$ and $FR^{1/2} = \sqrt{U^3/(g\nu)}$ gives

$$U = \left[\left(\frac{35\cos\alpha}{6\epsilon\sin^2\alpha}\right)^2 g\nu\right]^{1/3} \quad \text{and} \quad \delta = \frac{1}{a}\left[\frac{35\nu^2\cos\alpha}{6g\epsilon\sin^2\alpha}\right]^{1/3}. \tag{22}$$

We want to examine the effect of varying the helix curvature ϵ on the flow and, for this, we choose to keep the helix torsion $\tau = \epsilon\tan\alpha$ fixed at some small value (since the torsion is assumed to be small). Then, as ϵ decreases the helix slope $\tan\alpha$ must increase and we will still obtain a non-trivial free-surface shape. Thus we write

$$U = \left[\left(\frac{35}{6\tau\sin\alpha}\right)^2 g\nu\right]^{1/3} \quad \text{and} \quad \delta = \frac{1}{a}\left[\frac{35\nu^2}{6g\tau\sin\alpha}\right]^{1/3}, \tag{23}$$

where $\sin\alpha = \tau/\sqrt{\tau^2+\epsilon^2}$.

The typical values $\nu \simeq 10^{-6}\,\mathrm{m^2\,s^{-1}}$ (water), $a \simeq 0.5\,\mathrm{m}$, $\tau \simeq 0.1$, $\epsilon \simeq 0.5$ and $\sin\alpha \simeq 0.2$ give $\delta \simeq 6\times10^{-4}$, so that $\delta \ll 1$, as assumed. Also, for these values, $U \simeq 0.95\,\mathrm{m/s}$, the Reynolds number R and the reduced Reynolds number $\delta^2 R$ are of orders 10^6 and 10^{-1}, respectively, and F is of order 1.

The parameters of the full small-helix-torsion numerical model of Section II may also be expressed in terms of physical parameters:

$$\frac{R\sin\alpha}{F^2} = \left[\left(\frac{6\tau g a^3}{35\nu^2}\right)^2 \sin^5\alpha\right]^{1/3}, \quad \frac{R^2\cos\alpha}{F^2} = \frac{ga^3\epsilon\sin\alpha}{\nu^2\tau}, \quad K = 2\epsilon a^2\left[\left(\frac{35}{6\nu\tau\sin\alpha}\right)^2\frac{g}{\tau}\right]^{1/3}. \tag{24}$$

The dimensional flux Ua^2Q down the channel is given by

$$Ua^2Q = Ua^2\delta \sin\alpha\, \hat{Q} = \frac{35\nu a}{6\tau}\hat{Q}, \tag{25}$$

which is independent of the helix curvature ϵ. Thus, results for a given value $\mathcal{Q}$ of the dimensionless flux $\hat{Q}$ correspond to results for a given physical flux and we may examine how they change with changes in the helix curvature ϵ. Note that both of our dimensionless models require specification of values for three free parameters, which we choose to be ϵ, τ and δ. In particular, we will fix τ and δ, both of which must be small, and allow ϵ to vary from zero to unity.

C. Solution and verification of results

In general, solutions for $h(y)$ of the ODE (15) must be obtained numerically; this was done readily using an ODE solver in MATLAB, for a chosen value of a parameter such as h_ℓ. Then h and h^3 were integrated numerically to determine the corresponding values of $\hat{\Omega}$ and $\hat{Q}$ from (18) and (19), respectively, using one of the MATLAB (version R2009b) built-in quadrature functions; for accuracy we used the adaptive Gauss-Konrad quadrature function (`quadgk`). More specifically, starting with two initial guesses of the unknown fluid depth h_ℓ at the left-hand free-surface contact point, one for $\hat{Q} < \mathcal{Q}$ and one for $\hat{Q} > \mathcal{Q}$, where $\hat{Q} = \mathcal{Q}$ is the prescribed flux down the channel, the bisection method was employed to determine the location of the free-surface contact points for $\hat{Q} = \mathcal{Q}$ to within a small tolerance. The flow-domain area $\hat{\Omega}$ was then calculated, by numerical integration of h, and a grid was defined over the flow domain on which the remaining quantities were calculated. MATLAB's in-built contouring functions were used to plot streamlines and contours of the axial velocity and pressure.

In the particular case of a channel of rectangular cross-section treated in Section IV, the ODE (15) may be solved exactly, and the integration to determine $\hat{\Omega}$ and $\hat{Q}$ may be performed exactly.

In order to verify the thin-film approximation the flow-domain geometry from a solution of the thin-film model was imported into COMSOL Multiphysics, and a solution of the full small-helix-torsion model described in Section II was found for this geometry via the method described in Subsection II B. The parameters for the full model were chosen to be consistent

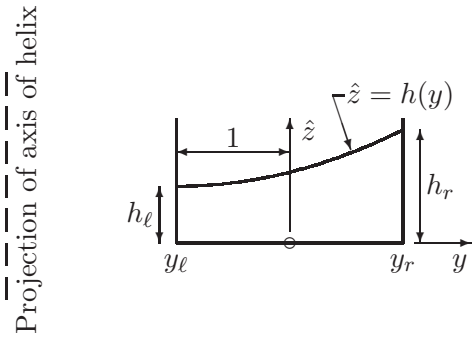

FIG. 3. Cross-section of a rectangular channel showing the locally Cartesian coordinate system with magnified z coordinate, $\hat{z} = z/\delta$. The x-axis is directed out of the figure in the direction of the primary axial flow.

with those used to obtain the thin-film solution. Specifically, for chosen values of the helix curvature and torsion, ϵ and τ, and the aspect ratio of the fluid domain, δ, we have

$$\frac{R\sin\alpha}{F^2} = \frac{\tau}{\delta^2\sqrt{\tau^2+\epsilon^2}}, \quad \frac{R^2\cos\alpha}{F^2} = \frac{35\epsilon}{6\tau^2\,\delta^3}, \quad K = \frac{2\epsilon(\tau^2+\epsilon^2)}{\delta^2}\left(\frac{35}{6\tau^2}\right)^2. \tag{26}$$

In general, the free-surface shape was adjusted a little from that obtained from the thin-film solution. The post-processing facilities provided by COMSOL were used to calculate the area of and flux through the updated flow domain. A quantitative indication of the accuracy of the thin-film model was obtained by comparing these quantities with those obtained from the thin-film solution.

IV. A CHANNEL OF RECTANGULAR CROSS-SECTION

Consider now the particular case of a channel of rectangular cross-section with left-hand and right-hand vertical walls at $y = y_\ell = -1$ and $y = y_r = 1$, as shown in Figure 3, for which $H(y) \equiv 0$ for $-1 < y < 1$. For this case the thin-film flow solution may be found exactly for a prescribed fluid depth at some position $y = y_0$ in the channel. Comparison of this solution with the numerical solution of the full small-helix-torsion model, for different values of the relevant parameters, verifies the thin-film model. Analysis of the exact thin-film solution for the channel of rectangular cross-section, for curvature between zero and unity and for flux ranging from zero to infinity, then provides insight into the flow behaviour not readily obtained from a numerical solution.

A. Thin-film solution

Let the fluid depth at the left and right vertical walls be $h(y_\ell) = h_\ell$ and $h(y_r) = h_r$,

which must, for prescribed curvature and flux, be determined as part of the solution. From (15) the film depth $h = h(y)$ satisfies

$$\frac{\mathrm{d}h}{\mathrm{d}y} = \frac{h^4}{1+\epsilon y}, \tag{27}$$

whose solution satisfying $h(-1) = h_\ell$ is

$$h = h_\ell \left[1 - \frac{3h_\ell^3}{\epsilon} \log\left(\frac{1+\epsilon y}{1-\epsilon}\right)\right]^{-1/3} \quad \text{for} \quad -1 \le y \le 1, \tag{28}$$

or alternatively whose solution satisfying $h(1) = h_r$ is

$$h = h_r \left[1 - \frac{3h_r^3}{\epsilon} \log\left(\frac{1+\epsilon y}{1+\epsilon}\right)\right]^{-1/3} \quad \text{for} \quad -1 \le y \le 1. \tag{29}$$

Equation (27) shows that h increases monotonically with y, and hence, in particular, that $h_\ell < h_r$; specifically, h_ℓ and h_r are related by

$$\frac{1}{h_\ell^3} - \frac{1}{h_r^3} = \eta, \tag{30}$$

in which we have defined

$$\eta = \frac{3}{\epsilon} \log\left(\frac{1+\epsilon}{1-\epsilon}\right), \tag{31}$$

so that $\eta \ge 6$ for $0 \le \epsilon < 1$. Note from (28) that, except in the limit $\epsilon \to 1$, in which $h(-1) \to 0$ (i.e. $h_\ell \to 0$), the fluid depth h is strictly positive within the channel $-1 \le y \le 1$, showing that the free surface never intersects the bed $\hat{z} = 0$ of the channel.

Substituting the solution (28) or (29) for h into (18) and (19) gives the flow-domain area $\hat{\Omega}$ and the flux $\hat{Q}$, respectively:

$$\hat{\Omega} = \frac{1+\epsilon}{3^{1/3}\epsilon^{2/3}} \exp\left(\frac{\epsilon}{3h_r^3}\right) \left[\Gamma\left(\frac{2}{3}, \frac{\epsilon}{3h_r^3}\right) - \Gamma\left(\frac{2}{3}, \frac{\epsilon}{3h_\ell^3}\right)\right], \tag{32}$$

$$\hat{Q} = \frac{1+\epsilon}{9} \exp\left(\frac{\epsilon}{3h_r^3}\right) \left[\Gamma\left(0, \frac{\epsilon}{3h_r^3}\right) - \Gamma\left(0, \frac{\epsilon}{3h_\ell^3}\right)\right], \tag{33}$$

where $\Gamma(a, z)$ denotes the incomplete gamma function, defined by

$$\Gamma(a, z) = \int_z^\infty t^{a-1} e^{-t}\, \mathrm{d}t. \tag{34}$$

Equations (30) and (33) determine h_ℓ and h_r when ϵ and $\hat{Q} = \mathcal{Q}$ are prescribed.

From (30) we see that for physically meaningful (i.e. finite and positive) h_r we require $h_\ell < \eta^{-1/3}$; equation (30) also shows that $h_r \to \infty$ and $\mathrm{d}h/\mathrm{d}y \to \infty$ as $h_\ell \to \eta^{-1/3}$, i.e. both the fluid depth and the free-surface slope at the right-hand wall become infinite in this limit. Thus there is a limiting value of h_ℓ, denoted by $h_{\ell\max} = h_{\ell\max}(\epsilon) = \eta^{-1/3}$ (and, as we shall see, a corresponding limiting value of $\hat{\Omega}$, denoted by $\hat{\Omega}_{\max} = \hat{\Omega}_{\max}(\epsilon)$), at and beyond which there is no physically meaningful solution.

B. Small-helix-curvature limit

At leading order in the limit of small helix curvature, $\epsilon \to 0^+$ (the case considered by Stokes et al. [24]), from (31) we have $\eta \to 6$ and from (28) we have

$$h = h_\ell \left(1 - 3h_\ell^3(1+y)\right)^{-1/3}. \tag{35}$$

Also the flow-domain area $\hat{\Omega}$ and the flux $\hat{Q}$ in (32) and (33) simplify to

$$\hat{\Omega} = \frac{1}{2h_\ell^2}\left[1 - \left(1 - 6h_\ell^3\right)^{2/3}\right], \quad \hat{Q} = -\frac{1}{9}\log\left(1 - 6h_\ell^3\right). \tag{36}$$

Prescribing the value of the flux $\hat{Q} = \mathcal{Q}$ we thus obtain h_ℓ and h_r in terms of $\mathcal{Q}$:

$$h_\ell = \left(\frac{1 - \exp(-9\mathcal{Q})}{6}\right)^{1/3}, \quad h_r = \left(\frac{\exp(9\mathcal{Q}) - 1}{6}\right)^{1/3}. \tag{37}$$

Therefore

$$h = \left[\frac{6}{1 - \exp(-9\mathcal{Q})} - 3(1+y)\right]^{-1/3}, \tag{38}$$

and hence

$$\hat{\Omega} = \left(\frac{3}{\sqrt{2}(1 - \exp(-9\mathcal{Q}))}\right)^{2/3}(1 - \exp(-6\mathcal{Q})). \tag{39}$$

In the limit of small flux $\mathcal{Q} \to 0$ we have $h_\ell \sim (3\mathcal{Q}/2)^{1/3} \to 0$, $h_r \sim (3\mathcal{Q}/2)^{1/3} \to 0$ and $\hat{\Omega} \sim (12\mathcal{Q})^{1/3} \to 0$, and in the limit of large flux $\mathcal{Q} \to \infty$ we have $h_\ell \to h_{\ell\max}(0) = 6^{-1/3} \simeq 0.5503$, $h_r \sim 6^{-1/3}\exp(3\mathcal{Q}) \to \infty$ and $\hat{\Omega} \to \hat{\Omega}_{\max}(0) = (9/2)^{1/3} \simeq 1.6510$. Note that h_ℓ, h_r and Ω are all monotonically increasing functions of the flux $\mathcal{Q}$, and so, in particular, $\hat{\Omega} < 1.6510$ for all $\mathcal{Q}$. Figure 4 shows the free-surface shape given by (35) for a range of values of h_ℓ. In particular, Figure 4 shows that the free-surface shape changes rapidly with h_ℓ as the latter approaches the limiting value $6^{-1/3}$.

C. Unit-helix-curvature limit

In the limit of unit helix curvature, $\epsilon \to 1^-$ (satisfying the physical requirement that $\epsilon < 1$), from (31) we have $\eta \to \infty$ and, since $0 < h_\ell < h_{\ell\max} = \eta^{-1/3} \to 0$, we see that $h_\ell = 0$ at leading order in the limit $\epsilon \to 1^-$. Moreover from (29)–(33) it may readily be seen that

$$h = h_r\left[1 - 3h_r^3\log\left(\frac{1+y}{2}\right)\right]^{-1/3} \tag{40}$$

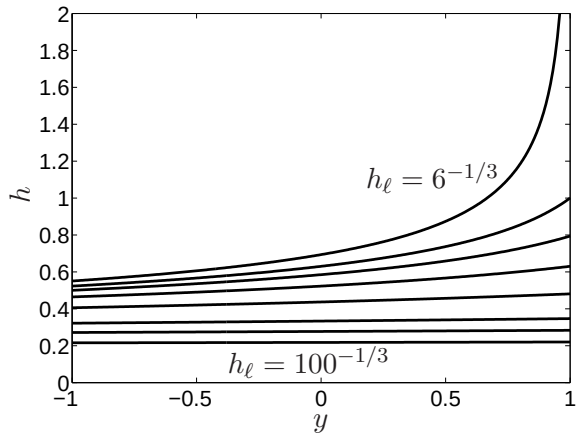

FIG. 4. Free-surface shape in the limit $\epsilon \to 0^+$ for $h_\ell^{-3} = 6$, 7, 8, 10, 15, 30, 50, 100, i.e. $h_\ell \simeq 0.55$, 0.52, 0.50, 0.46, 0.41, 0.32, 0.27, 0.22.

and

$$\hat{\Omega} = \frac{2}{3^{1/3}}\Gamma\left(\frac{2}{3}, \frac{1}{3h_r^3}\right)\exp\left(\frac{1}{3h_r^3}\right), \quad \hat{Q} = \frac{2}{9}\Gamma\left(0, \frac{1}{3h_r^3}\right)\exp\left(\frac{1}{3h_r^3}\right) \tag{41}$$

at leading order in the limit $\epsilon \to 1^-$. Prescribing the value of the flux $\hat{Q} = \mathcal{Q}$ in (41) gives h_r implicitly in terms of $\mathcal{Q}$. In the limit of small flux $\mathcal{Q} \to 0$ we have $h_r \sim (3\mathcal{Q}/2)^{1/3} \to 0$ and $\hat{\Omega} \sim (12\mathcal{Q})^{1/3} \to 0$, and in the limit of large flux $\mathcal{Q} \to \infty$ we have $h_r \sim 3^{-1/3}\exp(\gamma/3 + \mathcal{Q}/2) \to \infty$ (where $\gamma \simeq 0.5772$ is Euler's constant) and $\hat{\Omega} \to \hat{\Omega}_{\max}(1) = (2/3^{1/3})\Gamma(2/3) \simeq 1.8778$. Note that both h_r and Ω are monotonically increasing functions of the flux $\mathcal{Q}$, and so, in particular, $\hat{\Omega} < 1.8778$ for all $\mathcal{Q}$. Figure 5 shows the free-surface shape given by (40) for a range of values of h_r.

D. Verification of the thin-film model

In this Subsection we verify the thin-film solution for different values of the helix curvature ϵ (which, for the scaling used in our thin-film model, is the only free parameter in the problem for the free-surface shape) by comparing it with the numerical solutions of the full small-helix-torsion model described in Subsection II B. To do this we must choose values for the helix torsion and fluid-domain aspect ratio, which we fix to be $\tau = 0.1$ and $\delta = 0.1$. As we have already seen, the parameters ϵ, τ and δ are the only parameters needed in the thin-film and the full small-helix-torsion models. The initial flow-domain geometry for the COMSOL

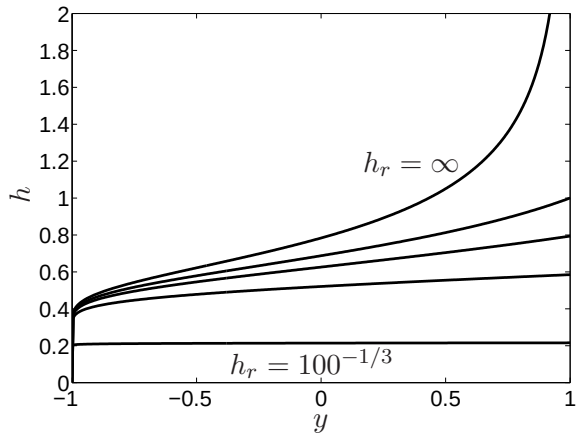

FIG. 5. Free-surface shape in the limit $\epsilon \to 1^-$ for $h_r^{-3} = 0$, 1, 2, 5, 100, i.e. $h_r \simeq \infty$, 1, 0.79, 0.58, 0.46, 0.22.

computation is that given by the thin-film model for prescribed flux $\mathcal{Q} = 0.1$. Since the free surface is, in general, modified by COMSOL, we also compare the flow-domain area and the flux of the two solutions. Because of the different scalings in the two models, we must use appropriate scalings of the results to make direct comparison between them possible. We have

$$z = \delta\,\hat{z}, \quad p = \frac{R}{\delta}\,\hat{p}, \quad \psi = \delta^2 R\,\hat{\psi}, \quad \Omega = \delta\,\hat{\Omega}, \quad Q = \delta \sin\alpha\,\hat{Q}, \tag{42}$$

where carets again denote variables of the thin-film model and

$$\delta^2 R = \left(\frac{35}{6\tau\sin\alpha}\right)\delta, \quad \frac{R}{\delta} = \left(\frac{35}{6\tau\sin\alpha}\right)\frac{1}{\delta^2}, \quad \sin\alpha = \frac{\tau}{\sqrt{\tau^2+\epsilon^2}}. \tag{43}$$

Since τ is held fixed as we vary ϵ, we have $\lim_{\epsilon\to 0^+}\sin\alpha = 1$ and $\lim_{\epsilon\to 1}\sin\alpha \simeq \tau$ for small torsion τ.

Figures 6–8 show the streamlines of the secondary flow, the axial velocity contours and the pressure contours, respectively, for both the full small-helix-torsion and the thin-film models with small helix curvature $\epsilon = 0.01$, while Figures 9–11 show the corresponding plots for large helix curvature $\epsilon = 0.9$. All of these figures also show the free-surface shapes predicted by both models. The agreement between the results of the two models is excellent. At the scale used, the free-surface shape and pressure contours are in remarkably good agreement, differing only near to the vertical channel walls. The axial velocity contours also agree extremely well, also differing only near to the vertical channel walls. The most

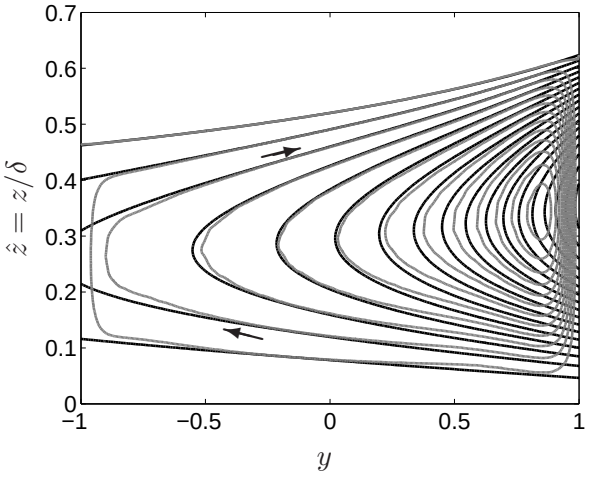

FIG. 6. Streamlines of the secondary flow, $\hat{\psi} = C \times 10^{-5}$ where $C = 0.0$ (outer curve), -0.2, -0.4, $\ldots$, -3.4 (inner curve), for a rectangular channel with helix curvature $\epsilon = 0.01$ and torsion $\tau = 0.1$. The aspect ratio of the flow domain is $\delta = 0.1$ and the flux is $\mathcal{Q} = 0.1$. Black curves correspond to the thin-film model and grey curves correspond to the full small-helix-torsion model. The arrows show the direction of the flow.

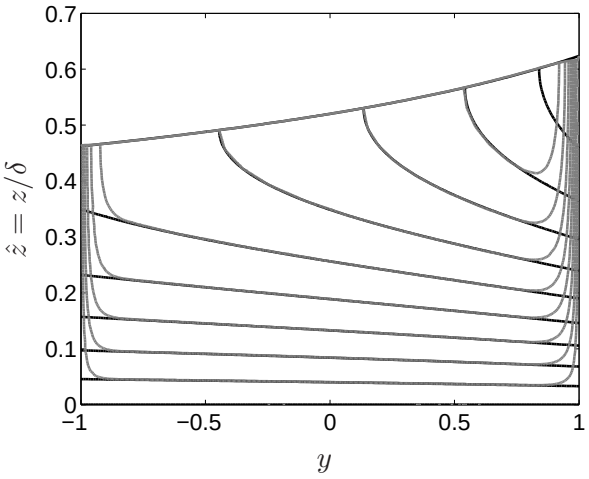

FIG. 7. Axial flow contours, $u = C \times 10^{-1}$ where $C = 0.0$ (lowest curve), 0.2, 0.4, $\ldots$, 1.8 (highest curve), for a rectangular channel with helix curvature $\epsilon = 0.01$ and torsion $\tau = 0.1$. The aspect ratio of the flow domain is $\delta = 0.1$ and the flux is $\mathcal{Q} = 0.1$. Black curves correspond to the thin-film model and grey curves correspond to the full small-helix-torsion model.

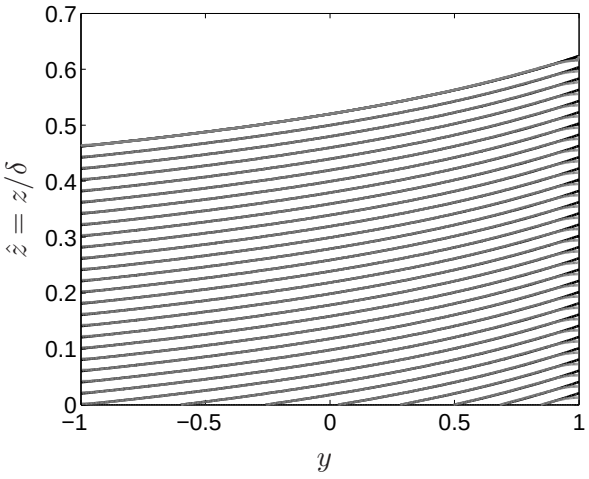

FIG. 8. Pressure contours, $\hat{p} = C \times 10^{-2}$ where $C = 0.0$ (highest curve), 0.2, 0.4, ..., 6 (lowest curve), for a rectangular channel with helix curvature $\epsilon = 0.01$ and torsion $\tau = 0.1$. The aspect ratio of the flow domain is $\delta = 0.1$ and the flux is $\mathcal{Q} = 0.1$. Black curves correspond to the thin-film model and grey curves correspond to the full small-helix-torsion model. The only discernible differences between the two sets of curves are at the right-hand channel wall.

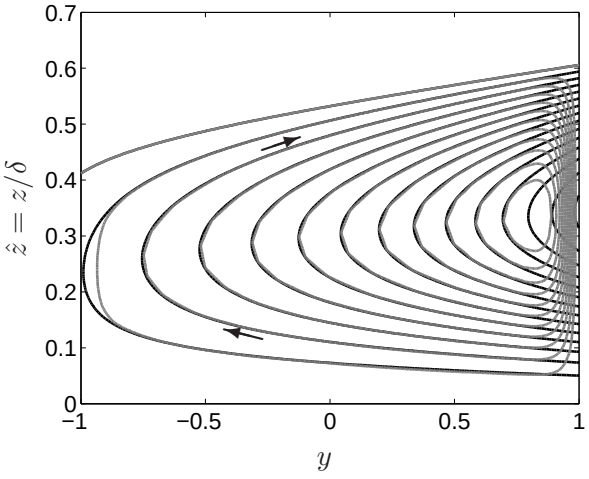

FIG. 9. Streamlines of the secondary flow, $\hat{\psi} = C \times 10^{-4}$ where $C = 0.0$ (outer curve), -0.2, -0.4, ..., -5.6 (inner curve), for a rectangular channel with helix curvature $\epsilon = 0.9$ and torsion $\tau = 0.1$. The aspect ratio of the flow domain is $\delta = 0.1$ and the flux is $\mathcal{Q} = 0.1$. Black curves correspond to the thin-film model and grey curves correspond to the full small-helix-torsion model. The arrows show the direction of the flow.

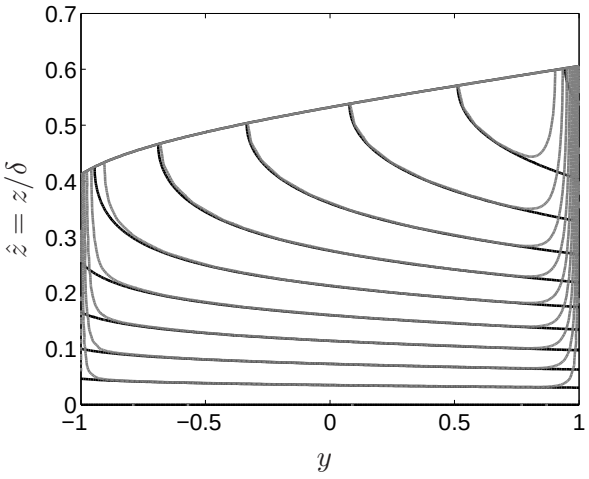

FIG. 10. Axial flow contours, $u = C \times 10^{-2}$ where $C = 0.0$ (lowest curve), 0.2, 0.4, ..., 4.2 (highest curve), for a rectangular channel with helix curvature $\epsilon = 0.9$ and torsion $\tau = 0.1$. The aspect ratio of the flow domain is $\delta = 0.1$ and the flux is $\mathcal{Q} = 0.1$. Black curves correspond to the thin-film model and grey curves correspond to the full small-helix-torsion model.

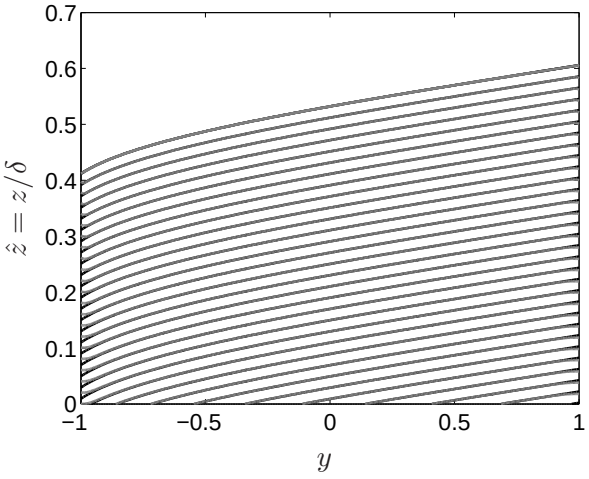

FIG. 11. Pressure contours, $\hat{p} = C \times 10^{-1}$ where $C = 0.0$ (highest curve), 0.2, 0.4, ..., 6 (lowest curve), for a rectangular channel with helix curvature $\epsilon = 0.9$ and torsion $\tau = 0.1$. The aspect ratio of the flow domain is $\delta = 0.1$ and the flux is $\mathcal{Q} = 0.1$. Black curves correspond to the thin-film model and grey curves correspond to the full small-helix-torsion model. The only discernible differences between the two sets of curves are at the two vertical channel walls.

	Thin-film model		Small-helix-torsion model	
ϵ	$\hat{\Omega}$	$\hat{Q} = \mathcal{Q}$	$\hat{\Omega}$	$\hat{Q}$
0.01	1.05485	0.10000	1.05486	0.096000
0.5	1.05489	0.10000	1.05501	0.096292
0.9	1.05291	0.10000	1.05347	0.096460

TABLE I. Comparison of the flow-domain area $\hat{\Omega}$ and the flux $\hat{Q}$ for the thin-film and full small-helix-torsion models.

significant differences between the predictions of the two models are in the streamlines. These differences are due to the fact that the thin-film model satisfies the no-slip boundary condition only along the bottom of the channel, while the no-slip conditions along the vertical channel walls are necessarily neglected. In reality there is a thin boundary layer along these walls which the thin-film model does not resolve, but which is shown in the solution to the full small-helix-torsion model. The thickness of these boundary layers reduces with the aspect ratio δ, and goes to zero in the thin-film limit, $\delta \to 0$. Hence the smaller the value of δ used for our full small-helix-torsion model, the better the agreement with the thin-film model should be. The effect of this boundary layer is greater at the right-hand wall of the channel, near to which the axial velocity in the thin-film model is largest, than at the left-hand wall, where it is smallest. Similar excellent agreement between the two models was found for $\epsilon = 0.5$, but this is not shown here for brevity. The agreement in the free-surface shape improves slightly as the helix curvature ϵ decreases.

The flow-domain area $\hat{\Omega}$ and flux $\hat{Q}$ predicted by each model for each of $\epsilon = 0.01$, 0.5 and 0.9 are shown in Table I. In all cases, the flux $\hat{Q}$ given by the full small-helix-torsion model is just a little less than the value $\hat{Q} = 0.1$ used to obtain the thin-film solution. This larger flux in the thin-film model corresponds to the neglect of the no-slip conditions on the vertical channel walls, as discussed above. The flow-domain areas $\hat{\Omega}$ agree very well.

E. Discussion of results

Having shown the thin-film model to be in good agreement with numerical solutions to the full small-helix-torsion model, we now use it to analyse further the flow in a rectangular

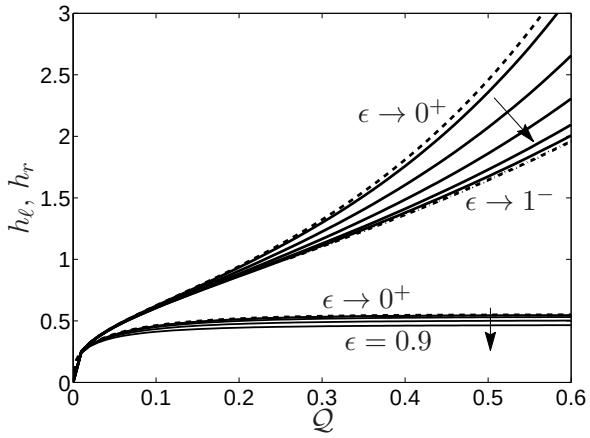

FIG. 12. Fluid depths at the left-hand and right-hand channel walls, h_ℓ and h_r, as functions of the prescribed flux $\mathcal{Q}$ in the asymptotic limits $\epsilon \to 0^+$ (dashed), $\epsilon \to 1^-$ (dash-dot) and for $\epsilon = 0.05$, 0.25, 0.5, 0.75, 0.9 (solid). The lower set of curves is for h_ℓ and the upper set for h_r. The arrows show the direction of increasing ϵ. Note that $h_\ell = 0$ for all $\mathcal{Q}$ at leading order in the limit $\epsilon \to 1^-$. h_ℓ and h_r are shown separately in Figures 13 and 14 for a larger range of $\mathcal{Q}$.

channel. The effects of both the helix curvature ϵ and the flux $\mathcal{Q}$ on the free-surface shape are of particular interest. Also of interest is how well the solutions in the limits $\epsilon \to 0^+$ and $\epsilon \to 1^-$ represent the solutions for small non-zero curvature and for curvature near to unity.

1. Fluid depth at the vertical channel walls

Figures 12–14 show the fluid depths at the left-hand and right-hand channel walls, h_ℓ and h_r, as functions of the prescribed flux $\mathcal{Q}$ for a range of values of the helix curvature ϵ. Figure 12 shows both h_ℓ and h_r over a relatively small range of $\mathcal{Q}$, and shows that h_ℓ quite quickly approaches its maximum value $h_{\ell\max} = \eta^{-1/3}$, with η given by (31), while h_r continues to increase without bound. Figures 13 and 14 show h_ℓ and h_r, respectively, over a larger range of $\mathcal{Q}$. Clearly the maximum value of h_ℓ has almost been reached by $\mathcal{Q} = 1$ for all values of ϵ shown. This is also shown in Figure 15, which shows $h_{\ell\max} = \eta^{-1/3}$ plotted as a function of ϵ, with crosses showing computed values of h_ℓ for $\mathcal{Q} = 1$ for a range of values of ϵ. From Figure 15 it is apparent that the computed value of the flux $\hat{Q}$ becomes very sensitive to the value of h_ℓ as it increases. Hence, as $\mathcal{Q}$ increases, h_ℓ needs to be

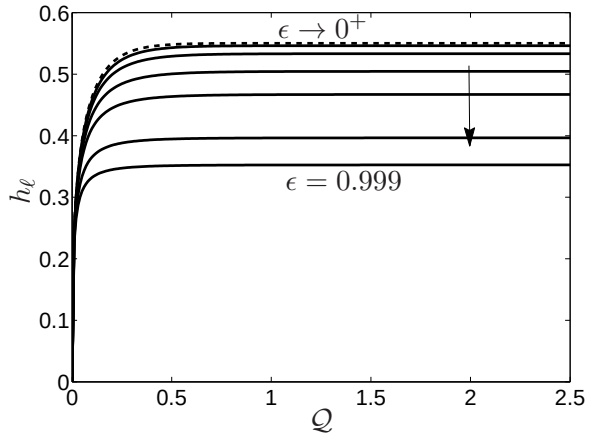

FIG. 13. Fluid depth at the left-hand channel wall, h_ℓ, as a function of the prescribed flux $\mathcal{Q}$ for the asymptotic limit $\epsilon \to 0^+$ (dashed) and for $\epsilon = 0.25$, 0.5, 0.75, 0.9, 0.99, 0.999 (solid). The arrow shows the direction of increasing ϵ. The curve for $\epsilon = 0.05$ cannot be distinguished from that for $\epsilon \to 0^+$ at the scale used. Note that $h_\ell = 0$ for all $\mathcal{Q}$ at leading order in the limit $\epsilon \to 1^-$.

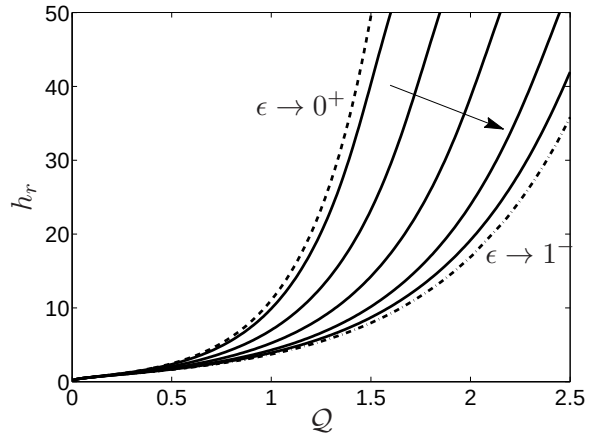

FIG. 14. Fluid depth at the right-hand channel wall, h_r, as a function of the prescribed flux $\mathcal{Q}$ in the asymptotic limits $\epsilon \to 0^+$ (dashed), $\epsilon \to 1^-$ (dash-dot) and for $\epsilon = 0.05$, 0.25, 0.5, 0.75, 0.9 (solid). The arrow shows the direction of increasing ϵ.

calculated to an increasingly higher precision. Eventually, for moderately large $\mathcal{Q}$ we reach the limits of numerical precision. For $\epsilon = 0.05$ this occurred at $\mathcal{Q} \simeq 3.5$, but for $\epsilon \geq 0.25$ it was possible to compute up to $\mathcal{Q} = 4$ (which was the largest value of $\mathcal{Q}$ considered) without significant loss of accuracy. For satisfactory numerical accuracy at these larger

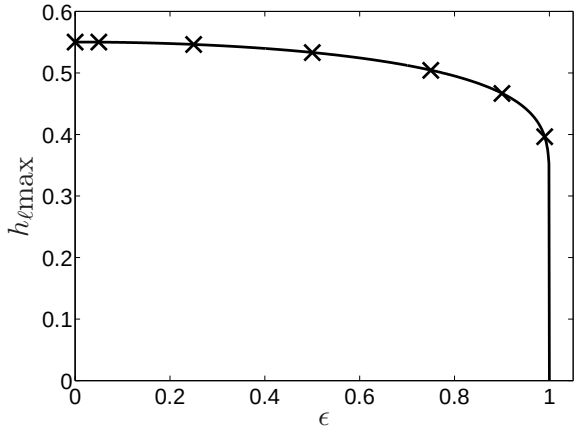

FIG. 15. The maximum possible fluid depth at the left-hand channel wall, $h_{\ell\max} = \eta^{-1/3}$, where $\eta = (3/\epsilon)\log((1+\epsilon)/(1-\epsilon))$, plotted as a function of the helix curvature ϵ. The crosses show the fluid depth h_ℓ for flux $\mathcal{Q} = 1$ in the asymptotic limit $\epsilon \to 0^+$ and for $\epsilon = 0.05$, 0.25, 0.5, 0.75, 0.9, 0.99.

values of the flux it was essential to compute $\hat{Q}$ using a quadrature function of sufficient accuracy. The trapezoidal rule was not suitable, but MATLAB's higher-order quadrature functions (namely, adaptive Simpson, adaptive Lobatto and adaptive Gauss-Konrod) all gave satisfactory results. The adaptive Gauss-Konrod function (`quadgk`) was selected for its accuracy and because it handles moderate singularities at the endpoints of the domain. Figures 12–14 also show that for $0 < \epsilon < 1$ the fluid depths h_ℓ and h_r are monotonically decreasing functions of the helix curvature ϵ and monotonically increasing functions of the flux $\mathcal{Q}$, satisfying $h_\ell \to 0$ and $h_r \to 0$ as $\mathcal{Q} \to 0$ and $h_\ell \to h_{\ell\max} = \eta^{-1/3}$ and $h_r \to \infty$ as $\mathcal{Q} \to \infty$, in accord with the behaviour in the limits $\epsilon \to 0^+$ and $\epsilon \to 1^-$ described earlier.

2. Flow-domain area

Figure 16 shows the flow-domain area, $\hat{\Omega}$, plotted as a function of the prescribed flux $\mathcal{Q}$ for a range of values of the helix curvature ϵ. In particular, Figure 16 shows that for $0 < \epsilon < 1$ the flow-domain area $\hat{\Omega}$ is a monotonically increasing function of the helix curvature ϵ and of the flux $\mathcal{Q}$, satisfying $\hat{\Omega} \to 0$ as $\mathcal{Q} \to 0$ and $\hat{\Omega} \to \hat{\Omega}_{\max}(\epsilon)$ as $\mathcal{Q} \to \infty$, again in accord with the behaviour in the limits $\epsilon \to 0^+$ and $\epsilon \to 1^-$ described earlier. In particular, this

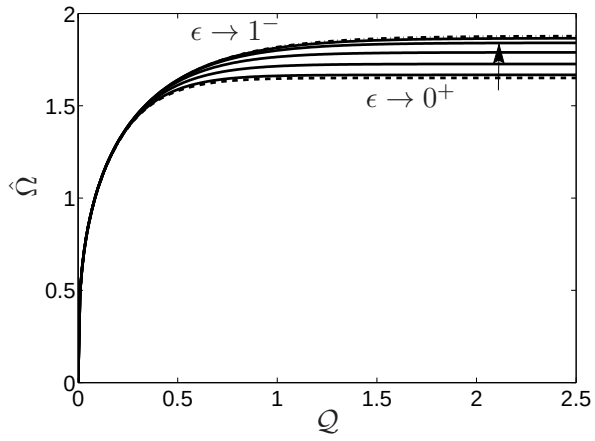

FIG. 16. Cross-sectional area of the flow domain $\hat{\Omega}$ as a function of the prescribed flux $\mathcal{Q}$ in the limits $\epsilon \to 0^+$ (dashed), $\epsilon \to 1^-$ (dash-dot) and for $\epsilon = 0.05, 0.25, 0.5, 0.75, 0.9$ (solid). The arrow shows the direction of increasing ϵ.

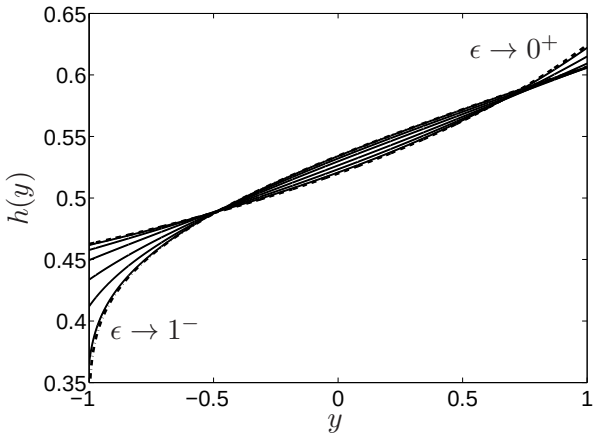

FIG. 17. Free-surface shape $h(y)$ for $\epsilon = 0.05, 0.25, 0.5, 0.75, 0.9, 0.99$ (solid) and in the limits $\epsilon \to 0^+$ (dashed) and $\epsilon \to 1^-$ (dash-dot) with flux $\mathcal{Q} = 0.1$.

means that $\hat{\Omega} < \hat{\Omega}_{\max}(1) \simeq 1.8778$ for all values of ϵ and $\mathcal{Q}$.

3. Free-surface shape

Figure 17 shows the free-surface shape $h(y)$ with prescribed flux $\mathcal{Q} = 0.1$ for a range of values of the helix curvature ϵ. In particular, Figure 17 shows how the curvature of the free

surface changes sign as ϵ increases. Differentiating (27) with respect to y we have

$$h'' = \frac{h^4(4h^3 - \epsilon)}{(1 + \epsilon y)^2}, \tag{44}$$

where a dash denotes differentiation with respect to argument, from which it is clear that the free-surface curvature (i.e. h'' in the thin-film approximation) changes sign when h passes through $(\epsilon/4)^{1/3}$. Substituting $h_\ell = (\beta\eta)^{-1/3}$, where $\beta \geq 1$ and η is given by (31), into (28) we find that

$$h'' \begin{array}{c} > \\ = \\ < \end{array} 0 \quad \text{for} \quad y \begin{array}{c} > \\ = \\ < \end{array} \zeta, \quad \text{where} \quad \zeta = \frac{1}{\epsilon}\left[\mathrm{e}^{-4/3}\left(\frac{1+\epsilon}{1-\epsilon}\right)^{\beta-1}(1+\epsilon) - 1\right], \tag{45}$$

i.e. that the curvature h'' changes sign from negative to positive at $y = \zeta$. In particular, as Figure 17 confirms, in the limit $\epsilon \to 0^+$ we have $\zeta \to -\infty$ and hence the curvature is always positive across the entire channel (in agreement with the solution in that limit described in Subsection IV B), while in the limit $\epsilon \to 1^-$ we have $\zeta \to +\infty$ and hence the curvature is always negative across the entire channel (in agreement with the solution in that limit described in Subsection IV C). As the helix curvature ϵ increases, the slope of the channel decreases because the helix torsion is held constant, and the free-surface shape changes from one resembling the paraboloidal shape generated by a forced (rotational) vortex, seen, for example, when a container of fluid is rotated about its axis, to one resembling that generated by a free (irrotational) vortex, seen, approximately, when water drains through a plug hole [30].

Figure 18 shows the free-surface shape $h(y)$ with fixed helix curvature, specifically $\epsilon = 0.99$, for a range of values of the prescribed flux $\mathcal{Q}$. Figure 18 also shows the asymptotic solution in the limit $\epsilon \to 1^-$ (which is, as expected, virtually indistinguishable for all values of $\mathcal{Q}$) and the asymptotic solution in the limit $\mathcal{Q} \to \infty$ given by (40) in the limit $h_r \to \infty$. In particular, Figure 18 shows that the free-surface shape in the limit $\mathcal{Q} \to \infty$ is very similar to that for $\mathcal{Q} = 1$, except near to the left-hand channel wall where, in the limit $\mathcal{Q} \to \infty$, the fluid depth drops rapidly to zero at the wall. In the case of near-unity helix curvature and large flux, the free-surface shape resembles that of a compound vortex [30]; near to the left-hand channel wall ($y = -1$) the free-surface shape is like that generated by a free vortex (with negative curvature) and, as y increases, its shape becomes like that generated by a forced vortex (with positive curvature). Using (40) we find that in the limit $\epsilon \to 1^-$, h'' changes from negative to positive at $y = 2\exp[(h_r^{-3} - 4)/3] - 1$. In particular, as Figure 18

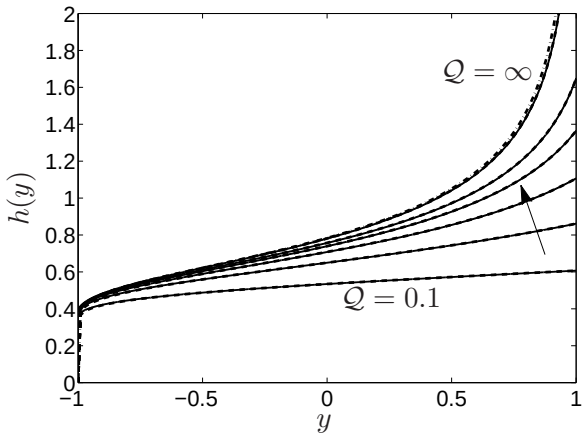

FIG. 18. Free-surface shape $h(y)$ for $\mathcal{Q} = 0.1$, 0.2, 0.3, 0.4, 0.5, 1 with $\epsilon = 0.99$. The arrow shows the direction of increasing $\mathcal{Q}$. The solid curves show predictions of the thin-film model and the dashed curves show the virtually indistinguishable asymptotic solution in the limit $\epsilon \to 1^-$. The asymptotic solution in the limit $\mathcal{Q} \to \infty$ curve (dash-dot) is given by (40) in the limit $h_r \to \infty$.

shows, in the limit $\mathcal{Q} \to \infty$ ($h_r \to \infty$) the sign of h'' changes at $y \simeq -0.4728$, while for $\mathcal{Q} \simeq 0.1$ ($h_r = 0.6$) $h'' < 0$ across the entire width of the channel, as shown by the curve for $\mathcal{Q} = 0.1$.

V. CONCLUSIONS

We developed a thin-film model for flows of small depth in helically-wound channels. The helix torsion was assumed to be small and the helix radius must be greater than the half-width of the channel. The channel may have any cross-sectional shape, and it was shown that the solution for the film depth as a function of horizontal position in the channel cross-section is governed by the first-order ODE (15) (which must, in general, be solved numerically). With the scaling used, the fluid depth (and therefore the free-surface shape) depends only on the helix curvature ϵ and the fluid depth at a given position, usually taken to be the left-hand end of the free surface. The volume flux down the channel is found by quadrature.

The present work focused on a channel with rectangular cross-section, for which an exact solution of (15) is available, greatly facilitating detailed analysis of the flow. We found that

there is a (finite) upper limit on the fluid depth at the left-hand channel wall, h_ℓ, dependent on the helix curvature, above which there is no physically meaningful solution. At this value of h_ℓ both the fluid depth and the slope of the free surface at the right-hand channel wall are infinite. The upper limit on h_ℓ corresponds to infinite flux down the channel, and so the range of possible values of h_ℓ covers all possible fluxes $\mathcal{Q}$ (i.e. ranging from zero to infinity). In the limit as the flux goes to infinity the flow-domain area also approaches a (finite) upper limit. Computed results for non-zero helix curvature show the same behaviour as in the limits of zero- and unit-helix-curvature.

An interesting feature of this problem is the change in the free-surface shape as the helix curvature increases to unity for fixed values of the flux and (small) helix torsion. If the helically-wound channel is viewed from above, the axial velocity component resembles that of a vortex flow. In the case of small flux, the free-surface shape at small helix curvature resembles that generated by a forced vortex; as the helix curvature increases it changes to resemble that generated by a free vortex. In the case of large flux the free-surface shape at small helix curvature still resembles that of a forced vortex; as the helix curvature increases the free-surface shape near the left-hand channel wall resembles that generated by a free vortex but changes to a shape resembling a forced vortex away from that wall, i.e. it has a shape consistent with a compound vortex. Given the helix curvature ϵ and the flux $\mathcal{Q}$, which determines the fluid depth at the left-hand vertical wall h_ℓ, we are able to determine from (45) whether the free surface has a shape corresponding to a free, forced, or compound vortex and, in the latter case, the inflexion point. In addition, the helix torsion is small. It is, then, not surprising that the flow has features of free, forced and compound vortex flow, as we have inferred from the free-surface shape. Note that our findings call into question the assumption made by Holland-Batt [11] of free vortex flow in the outer region of the channel. The validity of this assumption depends on the problem parameters, and for moderate to large flux the flow in the outer region of the channel looks more like that of a forced vortex than a free vortex. Where the helix torsion and curvature are small, as in Holland-Batt's more recent work on large diameter spiral separators of rectangular cross-section [25], the free-vortex assumption is not justified. The thin-film model presented in the current work provides an alternative means for predicting the flow within spiral separators that should be more accurate and more generally applicable, and is straightforward to use.

Corresponding results for channels whose cross-sectional shapes are other than rectangu-

lar may be obtained. In more typical cases (such as a channel of parabolic cross-section), the fluid depth at one or both points of contact of the free surface with the channel wall is zero and the horizontal position(s) of the contact point(s) must be found. In addition, it is in general no longer possible to obtain a closed-form solution of (15) or, in the few cases where an exact solution is available, its form often does not allow analysis of the flow to the extent possible for the rectangular case, so that behaviour must be inferred from numerical results, which presents some additional challenge.

Finally we note that the validity of the small-torsion assumption everywhere in the flow domain requires that $(A+y)^2+P^2 \gg aP$ for $y_\ell < y < y_r$. In particular, for the rectangular channel, as the curvature of the channel axis approaches unity ($\epsilon \to 1$) and $y_\ell \to -A$, torsion effects may be non-negligible in a region of the channel near to the vertical axis around which the channel is wound.

ACKNOWLEDGMENTS

Two extended visits by YMS to the University of Strathclyde were made possible by funding from the UK EPSRC (Research Grant GR/ S71873), the University of Adelaide Special Studies Program, and a University of Adelaide ECMS Faculty Grant.

Appendix A: Numerical solution of the full small-helix-torsion model

We here describe numerical solution of the full small-helix-torsion model of Section II, using the finite-element package COMSOL Multiphysics (version 3.5a). In order to implement the zero-stress boundary conditions (7c) and (8) in the standard finite-element manner, i.e. as the natural boundary conditions of the Navier–Stokes model, we add the y and z derivatives of the continuity equation (3) to (4b) and (4c), respectively, to obtain

$$v\frac{\partial v}{\partial y}+w\frac{\partial v}{\partial z}=-\frac{\partial p}{\partial y}+2\frac{\partial^2 v}{\partial y^2}+\frac{\partial}{\partial z}\left(\frac{\partial v}{\partial z}+\frac{\partial w}{\partial y}\right)+\frac{2\epsilon}{1+\epsilon y}\left(\frac{\partial v}{\partial y}-\frac{\epsilon v}{1+\epsilon y}\right)+\frac{Ku^2}{2(1+\epsilon y)}, \tag{A1a}$$

$$v\frac{\partial w}{\partial y}+w\frac{\partial w}{\partial z}=-\frac{\partial p}{\partial z}+\frac{\partial}{\partial y}\left(\frac{\partial w}{\partial y}+\frac{\partial v}{\partial z}\right)+2\frac{\partial^2 w}{\partial z^2}+\frac{\epsilon}{1+\epsilon y}\left(\frac{\partial v}{\partial z}+\frac{\partial w}{\partial y}\right)-\frac{R^2\cos\alpha}{F^2}, \tag{A1b}$$

which replace (4b) and (4c).

As discussed by Stokes [22, 23], it is necessary either to determine the points of contact of the free surface with the channel wall *a priori* or to have a means of varying them during the solution process. In the present work, considering flows of small depth, we use the thin-film model of Section III to define the initial flow domain for the numerical solution process and assume the contact points to be known *a priori*.

Next note that (4a), with boundary conditions $u = 0$ on the channel walls and (7a) on the free surface, has the form of a modified steady-state heat conduction-convection problem with u playing the role of temperature, while (3), (A1a) and (A1b), along with boundary conditions (5) on the channel walls and (7b) and (7c) on the free surface, comprise a modified two-dimensional steady-state Navier–Stokes problem. Thus, a heat conduction-convection model for the axial velocity (u) and a Navier–Stokes model for the secondary-flow components (v, w) and pressure (p) are set up within COMSOL Multiphysics. These are coupled through the three velocity components. In the special case of a straight channel, $\epsilon = 0$, these are standard models:

1. the heat conduction-convection equation with source term $R \sin\alpha/F^2$, "temperature" $u = 0$ on the channel walls and zero "heat conduction" through the free surface;

2. the Navier–Stokes equations with body force $(Ku^2/2, -R^2\cos\alpha/F^2)$, no slip and no penetration on the channel walls and zero stress conditions on the free surface.

In the general case of a curved channel, $\epsilon \neq 0$, the extra terms in (4a), containing the factor $\epsilon/(1+\epsilon y)$, must be explicitly added to the heat conduction-convection model for u, and the usual boundary condition at the free surface must be changed to allow non-zero heat conduction through it:

$$\frac{\partial u}{\partial y} n_y + \frac{\partial u}{\partial z} n_z = \frac{\epsilon u}{1+\epsilon y} n_y. \tag{A2}$$

With respect to the Navier–Stokes model for v, w, p, we first write the continuity equation (3) in the form

$$\frac{\partial v}{\partial y} + \frac{\partial w}{\partial z} + \frac{\epsilon v}{1+\epsilon y} = 0, \tag{A3}$$

showing that an extra term, $\epsilon v/(1+\epsilon y)$, must be added to the usual form of the continuity equation. Also, the additional terms in (A1a) and (A1b), containing the factor $\epsilon/(1+\epsilon y)$, must be explicitly added to the usual form of the Navier–Stokes equations and the body force changed slightly to $(Ku^2/(2(1+\epsilon y)), -R^2\cos\alpha/F^2)$.

Once the conduction-convection and Navier–Stokes models have been solved for the velocity and pressure, the flow-domain geometry is modified via a COMSOL Multiphysics moving mesh (augmented Lagrangian-Eulerian) model. This maps between fixed reference mesh coordinates (Y, Z) and the moving physical mesh coordinates (y, z). Motion of the physical mesh in the interior of the flow domain is determined by solving Laplace's equation for each of $y(Y, Z)$ and $z(Y, Z)$, subject to constraints on the boundary. At the channel walls the mesh does not move, while at the free surface the mesh moves according to the normal velocity component. An iterative procedure of solving for velocity and pressure, and then using this to update the physical mesh, is run until the kinematic condition (8) is satisfied. The kinematic condition is considered to be satisfied when

$$\int_\Gamma (vn_y + wn_z)^2 \, \mathrm{d}s < \texttt{tol}, \tag{A4}$$

where Γ denotes the boundary of the flow domain, s denotes arc length along Γ, and `tol` is a small tolerance of order 10^{-4} or less.

Finally, we also determine the stream function ψ defined by (9). In order to obtain ψ at all mesh nodes for export to MATLAB and to plot streamlines for comparison with those obtained from the thin-film model, the stream function is found by solving Poisson's equation

$$\frac{\partial^2 \psi}{\partial y^2} + \frac{\partial^2 \psi}{\partial z^2} = -\left[(1 + \epsilon y)\omega + \epsilon w\right], \tag{A5}$$

where $\omega = \partial w/\partial y - \partial v/\partial z$ is the component of vorticity in the direction of the primary flow.

In summary, the numerical solution to the present helically-symmetric small-torsion model is found, using COMSOL Multiphysics, by the iterative solution of four sub-problems: (1) a convection-conduction model for the primary flow velocity, (2) a Navier–Stokes model for the secondary flow velocity and pressure, (3) a moving mesh problem for updating the flow-domain geometry, and (4) Poisson's equation for the stream function. The initial flow-domain geometry used is that predicted by the thin-film model, which is adjusted a little by the iterative numerical solution process.

---

[1] Germano, M., "On the effect of torsion on a helical pipe flow", *J. Fluid Mech.* **125**, 1 (1982).

[2] Berger, S.A., Talbot, L. and Yao, L.-S., "Flow in curved pipes", *Ann. Rev. Fluid Mech.* **15**, 461 (1983).

[3] Kao, H.C., "Torsion effect on fully developed flow in a helical pipe", *J. Fluid Mech.* **184**, 335 (1987).

[4] Germano, M., "The Dean equations extended to a helical pipe flow", *J. Fluid Mech.* **203**, 289 (1989).

[5] Zabielski, L. and Mestel, A.J., "Steady flow in a helically symmetric pipe", *J. Fluid Mech.* **370**, 297 (1998).

[6] Thomson, J., "On the origin of windings of rivers in alluvial plains, with remarks on the flow of water round bends in pipes", *Proc. R. Soc. Lond. (1854–1905)* **25**, 5 (1876).

[7] Thomson, J., "Experimental demonstration in respect to the origin of windings of rivers in alluvial plains, and to the mode of flow of water round bends of pipes", *Proc. R. Soc. Lond. (1854–1905)* **26**, 356 (1877).

[8] Thomson, J., "On the flow of water in uniform régime in rivers and other open channels", *Proc. R. Soc. Lond. (1854–1905)* **28**, 114 (1878).

[9] Morton, F., King, P.J. and McLaughlin, A., "Helical-coil distillation columns. Part I: Efficiency studies", *Trans. Instn Chem. Engrs* **42**, T285 (1964).

[10] Morton, F., King, P.J. and McLaughlin, A., "Helical-coil distillation columns. Part II: Liquid film resistance", *Trans. Instn Chem. Engrs* **42**, T296 (1964).

[11] Holland-Batt, A.B., "Spiral separation: theory and simulation", *Trans. Instn Min. Metall. (Sect C: Mineral Process. Extr. Metall.)* **98**, C46 (1989).

[12] Holtham, P.N., "Flow visualisation of secondary currents on spiral separators", *Miner. Eng.* **3**, 279 (1990).

[13] Holland-Batt, A.B. and Holtham, P.N., "Particle and fluid motion on spiral separators", *Miner. Eng.* **4**, 457 (1991).

[14] Holtham, P.N., "Primary and secondary fluid velocities on spiral separators", *Miner. Eng.* **5**, 79 (1992).

[15] Wang J.-W. and Andrews, J.R.G., "Numerical simulations of liquid flow on spiral concentrators", *Miner. Eng.* **7**, 1363 (1994).

[16] Jancar, T., Fletcher, C.A.J., Holtham, P.N. and Reizes, J.A., "Computational and experimental investigation of spiral separator hydrodynamics", *Proc. XIX Int. Mineral Proc. Congress*,

SME 1995, p. 147–151.

[17] Matthews, B.W., Fletcher, C.A.J. and Partridge, A.C., "Computational simulation of fluid and dilute particulate flows on spiral concentrators", *Appl. Math. Model.* **22**, 965 (1998).

[18] Matthews, B.W., Fletcher, C.A.J., Partridge, A.C. and Vasquez, S., "Computation of curved free surface water flow on spiral concentrators", *J. Hydraul. Eng.* **125**, 1126 (1999).

[19] Batchelor, G.K., *An Introduction to Fluid Dynamics* (Cambridge University Press, Cambridge, 1967).

[20] Wilson, S.K. and Duffy, B.R., "On the gravity-driven draining of a rivulet of viscous fluid down a slowly varying substrate with variation transverse to the direction of flow", *Phys Fluids* **10**, 13 (1998).

[21] Wilson, S.K. and Duffy, B.R., "A rivulet of perfectly wetting fluid draining steadily down a slowly varying substrate", *IMA J. Appl. Math.* **70**, 293 (2005).

[22] Stokes, Y.M., "Flow in spiral channels of small curvature and torsion", in *IUTAM Symposium on Free Surface Flows*, edited by A.C. King and Y.D. Shikhmurzaev (Kluwer, Dordrecht, 2001), p. 289–296.

[23] Stokes, Y.M., "Computing flow in a spiral particle separator", *Proceedings of the 14th Australasian Fluid Mechanics Conference*, edited by B.B. Dally (Causal Productions, Adelaide, 2001), p. 677–680.

[24] Stokes, Y.M., Wilson, S.K. and Duffy, B.R., "Thin-film flow in open helically-wound channels", *Proceedings of the 15th Australasian Fluid Mechanics Conference*, edited by M. Behnia, W. Lin and G.D. McBain, (The University of Sydney, Sydney, 2004), Paper AFMC00187.

[25] Holland-Batt, A.B., "A method for the prediction of the primary flow on large diameter spiral troughs", *Miner. Eng.* **22**, 352 (2009).

[26] Weldon, B., "Fine coal beneficiation: spiral separators in the Australian industry", *Australian Coal Review* **4**, 25 (1997).

[27] Dean, W.R., "The streamline motion of flow in a curved pipe", *Phil. Mag.* **5**, 673 (1928).

[28] Reddy, J.N. and Gartling D.K., *The Finite Element Method in Heat Transfer and Fluid Dynamics* (CRC Press, Inc., Boca Raton, 1994).

[29] Yuan, S.W., *Foundations of Fluid Mechanics* (Prentice Hall, New Jersey, 1967) Appendix A.

[30] Childs, P.R.N., *Rotating Flows* (Elsevier Inc., Oxford, 2011) Chap. 3, 53–79.